

Parameters of the eclipsing binary α Draconis observed by *TESS* and *SONG*

Daniel R. Hey,^{1,2*} Angela Kochoska,³ Richard Monier,⁴ Oleg Kochukhov,⁵
 Cole Johnston,^{6,7} Timothy R. Bedding,^{1,2} Simon J. Murphy,^{1,2} Michael Abdul-Masih,⁸
 John Southworth,⁹ Mads Fredslund Andersen,² Frank Grundahl,² and Pere L. Pallé¹⁰

¹*School of Physics, Sydney Institute for Astronomy (SIfA), The University of Sydney, NSW 2006, Australia*

²*Stellar Astrophysics Centre, Department of Physics and Astronomy, Aarhus University, DK-8000 Aarhus C, Denmark*

³*Department of Astrophysics and Planetary Science, Villanova University, 800 East Lancaster Avenue, Villanova, PA 19085, USA*

⁴*LESIA, UMR 8109, Observatoire de Paris et Université Pierre et Marie Curie Sorbonne Universités, place J. Janssen, Meudon, France*

⁵*Department of Physics and Astronomy, Uppsala University, Box 516, SE-75120 Uppsala, Sweden*

⁶*Institute of Astronomy, KU Leuven, Celestijnenlaan 200D, 3001 Leuven, Belgium*

⁷*Department of Astrophysics, IMAPP, Radboud University Nijmegen, P. O. Box 9010, 6500 GL Nijmegen, the Netherlands*

⁸*European Southern Observatory, Alonso de Cordova 3107, Vitacura, Casilla 19001, Santiago de Chile, Chile*

⁹*Astrophysics Group, Keele University, Staffordshire, ST5 5BG, UK*

¹⁰*Instituto de Astrofísica de Canarias, E-38200 La Laguna, Tenerife, Spain*

Accepted XXX. Received YYY; in original form ZZZ

ABSTRACT

We present an analysis of the eclipsing single-lined spectroscopic binary system α Dra based on photometry from the *TESS* mission and newly acquired spectroscopic measurements. Recently discovered to have eclipses in the *TESS* data, at a magnitude of $V = 3.7$, α Dra is now one of the brightest detached eclipsing binary systems known. We obtain the parameters of this system by simultaneously fitting the *TESS* light curve in conjunction with radial velocities acquired from the *SONG* spectrograph. We determine the fractional radii (R/a) for the primary and secondary components of the system to be 0.0479 ± 0.0003 and 0.0226 ± 0.0005 respectively. We constrain the temperature, mass, and luminosity ($\log(L/L_{\odot})$) of the primary to be 9975 ± 125 K, $3.7 \pm 0.1 M_{\odot}$, and 2.49 ± 0.02 respectively using isochrone fitting. Although the secondary is too faint to appear in the spectra, the obtained mass function and observed inclination yields a secondary minimum mass of $M_2 = 2.5 \pm 0.1 M_{\odot}$, which suggests that it is an A2V type star. We were unable to obtain radial velocities of the secondary, and are only able to see a weak highly rotationally broadened absorption line, indicating that the secondary is rapidly rotating ($v \sin i \sim 200$ km/s). We also perform an abundance analysis of the primary star for 21 chemical elements. We find a complex abundance pattern, with a few elements having mild under-abundances while the majority have solar abundances. We make available the Python code used in this paper to facilitate future modelling of eclipsing binaries. 

Key words: binaries: eclipsing – stars: chemically peculiar – stars: fundamental parameters

1 INTRODUCTION

Eclipsing binaries (EBs) are fundamental to modern astrophysics. They offer an accurate, unbiased method for determining stellar parameters with high precision, and are our primary source of empirical measurements of the masses and radii of normal stars (Andersen 1991; Torres et al. 2010). Masses and radii can be determined to high accuracy from combined analysis of the light and radial velocity (RV) curves (Maxted et al. 2020), which are then used to calibrate models of stellar evolution (Stassun et al. 2009; Higl & Weiss 2017).

α Draconis (Thuban; HR 5291; TIC 165991532, hereafter, α Dra) is a well-studied single-lined spectroscopic binary (SB1). Recent observations by the Transiting Exoplanet Survey Satellite (*TESS*) showed that α Dra exhibits clear grazing eclipses that had previously gone unnoticed (Bedding et al. 2019). With knowledge of α Dra predating modern civilization, the recent discovery of eclipses is quite remarkable and highlights the advantage of continuous space-based photometric monitoring. In fact, α Dra has been closely studied in the literature since at least Campbell & Curtis (1903). This is largely a result of its brightness: at $V = 3.68$ magnitude α Dra is easily visible with the naked eye. α Dra is metal-deficient and belongs to the rare class of A0 III stars, with an apparent minor enhancement of Si and Cr which has not been con-

* E-mail: daniel.hey@sydney.edu.au

firmed by later observations (Renson & Manfroid 2009b). α Dra is one of the most well-known of the A0 III spectral type (the other being α Sextantis) to the point that it serves as a standard MK class star. With only two other A0 III stars known to exist in an eclipsing system, α Dra provides a near ideal environment to study this spectral type.

In this paper, we analyse *TESS* photometry and simultaneous high-resolution spectroscopic measurements taken with the Stellar Observations Network Group (*SONG*) spectrograph (Sec. 2). We characterise the system using the eclipsing binary softwares *ELLIC* and *PHOEBE* to obtain fundamental parameters of the system (Sec. 3). Finally, we analyse the primary and perform an abundance analysis on archival spectra, finding that most elements have near solar abundance (Sec. 4).

2 OBSERVATIONS

2.1 *TESS* photometry

The NASA Transiting Exoplanet Survey Satellite (*TESS*; Ricker et al. 2014) is an all-sky photometric survey satellite whose primary mission is to discover Earth-sized transiting exoplanets. *TESS* has four cameras which cover a total field of view of 24° by 96° that extends from the ecliptic pole to the ecliptic plane. It has surveyed both ecliptic hemispheres each for one year in 13 sectors. Each sector is observed for around 27 d. Since there is some overlap between sectors, some stars were observed during multiple sectors, especially if they lie close to the ecliptic pole.

TESS observed α Dra at 2-min cadence in five non-contiguous sectors: 14, 15, 16, 21, and 22. We downloaded the target pixel files from the Mikulski Archive for Space Telescopes (MAST), and extracted a simple aperture photometry (SAP) light curve by summing up the flux from each pixel contained within the default aperture mask. We did not make use of the *TESS* pipeline, which provides automatically extracted and cleaned light curves (Pre-Search Data Conditioning; Smith et al. 2012), since it is known to cause anomalous peaks when correcting the light curves of detached eclipsing binaries. Instead, we corrected our light curve with a spline of degree 5 fitted individually to the out-of-eclipse regions of each sector. We then interpolated the spline fit across the entire light curve, eclipses included, and corrected and normalised the light curve. We removed 3σ outliers prior to the spline fit. We show these corrections and the final light curve in Fig. 1 as well as the *TESS* aperture mask used to obtain the light curve.

2.2 High-resolution spectroscopy

We obtained 61 high resolution spectra of α Dra using the *SONG* spectrograph mounted on the 1.0 m robotic Hertzprung *SONG* telescope at the Teide Observatory in Tenerife (Andersen et al. 2014, 2019). The *SONG* spectrograph is a high resolution Åchelle spectrograph operating in the wavelength range of 4400–6900 Å. Several exposures were obtained during primary eclipse and one during secondary, to explore any potential Rossiter-McLaughlin effects present in the system. All exposures were obtained at the highest resolution ($R = 110,000$). The orbital phases at which spectra were obtained is shown in Fig. 2, with the observing information collected in Table 1.

To obtain radial velocities (RVs) of the primary, we normalized the spectra to the continuum by fitting a third-order polynomial to the upper 95th percentile of each spectral order. We then divided the

Table 1. Spectroscopic observation log of α Dra.

UTC Date (yy/mm/dd)	BJD (day)	Orbital phase	SNR	RV (km/s)
2019-10-28	2458785.3134	0.475	86	4.3 ± 0.1
2019-11-01	2458788.7821	0.543	103	26.6 ± 0.1
2019-11-17	2458804.6782	0.852	115	-29.6 ± 0.1
2019-11-25	2458812.7061	0.008	59	-40.9 ± 0.1
2019-11-28	2458815.6997	0.066	138	-40.5 ± 0.1
2019-11-29	2458816.7830	0.087	128	-40.3 ± 0.1
2019-11-30	2458817.6497	0.104	119	-39.9 ± 0.1
2019-12-01	2458818.6397	0.123	127	-39.1 ± 0.1
2019-12-04	2458821.6927	0.183	145	-36.3 ± 0.1
2019-12-08	2458825.6532	0.260	107	-30.6 ± 0.1
2019-12-10	2458827.6502	0.298	117	-26.7 ± 0.1
2019-12-11	2458828.6200	0.317	114	-24.8 ± 0.1
2019-12-12	2458829.7898	0.340	112	-22.0 ± 0.1
2019-12-13	2458830.6016	0.356	93	-19.7 ± 0.1
2019-12-14	2458831.6115	0.376	127	-16.7 ± 0.1
2019-12-20	2458837.6224	0.492	121	9.4 ± 0.1
2019-12-21	2458838.6407	0.512	140	15.7 ± 0.1
2019-12-22	2458839.5728	0.530	113	21.8 ± 0.1
2020-01-04	2458852.7108	0.786	122	-13.5 ± 0.1
2020-01-05	2458853.5553	0.802	123	-18.6 ± 0.1
2020-01-06	2458854.5305	0.821	107	-23.8 ± 0.1
2020-01-12	2458860.5458	0.938	115	-38.9 ± 0.1
2020-01-13	2458861.5191	0.957	111	-39.9 ± 0.1
2020-01-15	2458863.5105	0.996	96	-41.0 ± 0.1
2020-01-16	2458864.5086	0.015	108	-41.1 ± 0.1
2020-01-17	2458865.5024	0.035	125	-41.1 ± 0.1
2020-01-18	2458866.5237	0.054	112	-41.4 ± 0.1
2020-01-18	2458867.4961	0.073	105	-40.7 ± 0.1
2020-01-24	2458872.5447	0.172	129	-37.2 ± 0.1
2020-01-26	2458874.5474	0.210	151	-34.6 ± 0.1
2020-01-27	2458875.5441	0.230	125	-33.1 ± 0.1
2020-01-28	2458876.5452	0.249	149	-31.6 ± 0.1
2020-01-29	2458877.5674	0.269	111	-30.1 ± 0.1
2020-01-30	2458878.5294	0.288	109	-28.3 ± 0.1
2020-01-31	2458879.5290	0.307	98	-26.0 ± 0.1
2020-02-01	2458880.7203	0.331	105	-23.6 ± 0.1
2020-02-02	2458881.5312	0.346	127	-21.5 ± 0.1
2020-02-06	2458885.5133	0.424	94	-7.7 ± 0.1
2020-02-07	2458886.5115	0.443	116	-4.0 ± 0.1
2020-02-08	2458887.5069	0.463	149	0.9 ± 0.1
2020-02-09	2458888.8044	0.488	142	7.6 ± 0.1
2020-02-10	2458889.7604	0.506	151	13.4 ± 0.1
2020-02-11	2458890.5264	0.521	115	18.5 ± 0.1
2020-02-12	2458891.5308	0.541	133	25.5 ± 0.1
2020-02-13	2458892.5064	0.560	76	33.1 ± 0.1
2020-02-14	2458893.5199	0.579	135	41.1 ± 0.1
2020-02-15	2458895.4958	0.618	101	53.6 ± 0.1
2020-02-16	2458896.4804	0.637	108	55.7 ± 0.1
2020-02-17	2458897.4926	0.657	101	52.7 ± 0.1
2020-02-18	2458898.4802	0.676	148	44.8 ± 0.1
2020-02-19	2458899.4838	0.695	148	33.4 ± 0.1
2020-02-21	2458901.4682	0.734	124	10.8 ± 0.1
2020-02-22	2458901.5144	0.735	130	10.4 ± 0.1
2020-02-22	2458901.5577	0.736	146	9.9 ± 0.1
2020-02-22	2458901.5873	0.736	136	9.6 ± 0.1
2020-02-22	2458901.6165	0.737	138	9.3 ± 0.1
2020-02-22	2458901.6418	0.737	127	8.7 ± 0.1
2020-02-22	2458901.6738	0.738	129	8.1 ± 0.1
2020-02-22	2458901.6937	0.738	131	7.7 ± 0.1

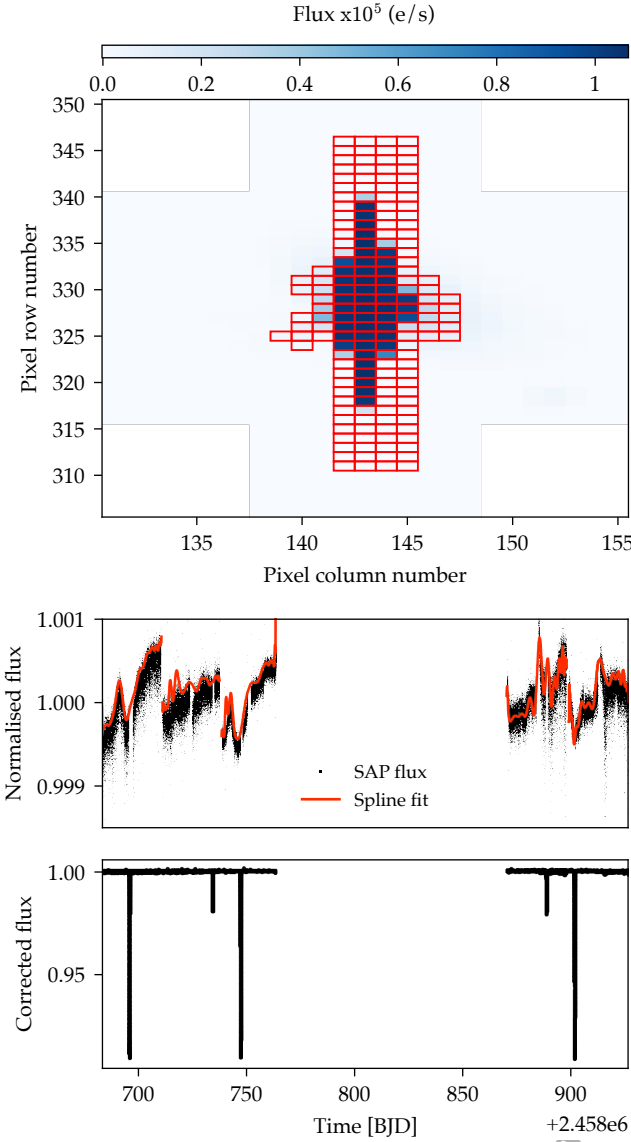


Figure 1. Top: The *TESS* target pixel file of α Dra for the first sector in which it was observed (14). The highlighted grey area shows the pixels used to produce the simple aperture photometry light curve from the *TESS* pipeline. Middle: The uncorrected flux with eclipses removed. The red lines are the spline fits. Bottom: The final corrected light curve after dividing through by the spline fit, with the eclipses included. [🔗](#)

flux of each order by this fit, and re-sampled the spectra to a constant log wavelength step of 0.02 \AA . The orders of each spectrum were then merged and cross-correlated against the first spectrum in the series (a ‘template’ spectrum). RVs were then derived from this cross-correlation by fitting a 1D Gaussian curve between -200 and 200 km/s . From these initial RVs, we constructed a refined template spectrum by shifting and stacking all 61 spectra to the primary reference frame. We repeated the cross-correlation for the new template spectrum, constructing a new template at each iteration until the difference between the current and previous extracted RVs was less than 0.01 m/s . We then converted the relative RVs to absolute RVs by cross-correlating the final primary template spectrum with an atomic linelist bundled with the *iSPEC* software (Blanco-Cuaresma et al. 2014) generated for an A0 type star. We extracted the radial velocities only within the wavelength regions

between 5030 to 5350 \AA , which we found to have the sharpest absorption lines.

In addition to our RVs, we also used those of Bischoff et al. (2017) to supplement our own measurements. The Bischoff et al. (2017) RVs were taken just over 3.5 years before our *SONG* measurement, and they greatly increase the precision on the orbital ephemeris. Although Adelman et al. (2001) also provided RVs, they have significantly more scatter than the other RV data, and were thus excluded from our analysis.

α Dra is well known to be a SB1, so only the fractional radii (R/a) can be determined from a combined light curve and RV analysis. To measure the absolute radii of the components requires RV measurements of the secondary, which would allow us to constrain the semi-major axis of the orbit. We thus attempted to find spectral lines from the secondary by shifting and stacking the spectra to the reference frame of the primary. We constructed a high SNR primary spectrum by taking the median spectrum of all shifted and stacked spectra. This spectrum was then subtracted from each individual spectrum, which were then cross-correlated with each other to show possible variations caused by the secondary. While we observed some residual signal in the cross-correlation, we were unable to derive radial velocities of the secondary star. This is not surprising – Behr et al. (2009) suggest that the secondary star accounts for less than 15% of the total luminosity of the system. This estimate agrees with direct interferometric measurement of a $1.83 \pm 0.07 \text{ mag}$ difference at $\lambda = 7000 \text{ \AA}$ by Hutter et al. (2016). Additionally, Kallinger et al. (2004) found that the signature of the secondary is only marginally visible. Using the high-quality *SOPHIE* spectrum we found a possible contribution of the secondary star in the vicinity of the strongest metal lines (Ca II 3933, Mg II 4481 \AA) (Fig. 3). These faint and broad features, indicating the secondary’s $v \sin i \sim 200 \text{ km s}^{-1}$, are red-shifted relative to the primary, which agrees with the orbital solution derived below. However, these lines are too faint to be reliably measured in the lower SNR *SONG* spectra.

We then attempted to disentangle the spectra using two independent spectral disentangling routines to obtain the signal for the secondary component. The first technique employed is a grid based iterative shift and stack routine (for an in depth discussion see e.g. Pavlovski & Hensberge 2010; Mahy et al. 2012; Shenar et al. 2020). As described above, this process involves first shifting all of the spectra to the reference of the primary and constructing a high SNR primary spectrum and then subtracting it from each individual spectrum. In this case however, instead of calculating a cross-correlating the residual spectra, we shifted all of the residual spectra to the reference of the secondary based on an assumed secondary semi-amplitude. A secondary spectrum was then constructed and subtracted from the original individual spectrum, and then this process was continued iteratively until the changes between iterations were negligible. A χ^2 value was then determined by reconstructing the individual spectra from the disentangled primary and secondary spectra and comparing the reconstructed spectra to the observations. This was done over a grid of secondary semi-amplitudes in order to find an optimal secondary semi-amplitude. While there was some structure in the χ^2 of the secondary semi-amplitude, the resulting secondary spectra did not show any discernible stellar features.

The second technique employed was *FDBINARY* (Ilijic et al. 2004), which unlike the shift and stack technique, operates in Fourier space (for an in depth discussion see e.g. Hadrava 1995; Ilijic et al. 2004; Pavlovski & Hensberge 2010). Based on a subset of orbital parameters, the remaining unknown orbital parameters can be determined. In this case, we left the semi-amplitude of the secondary

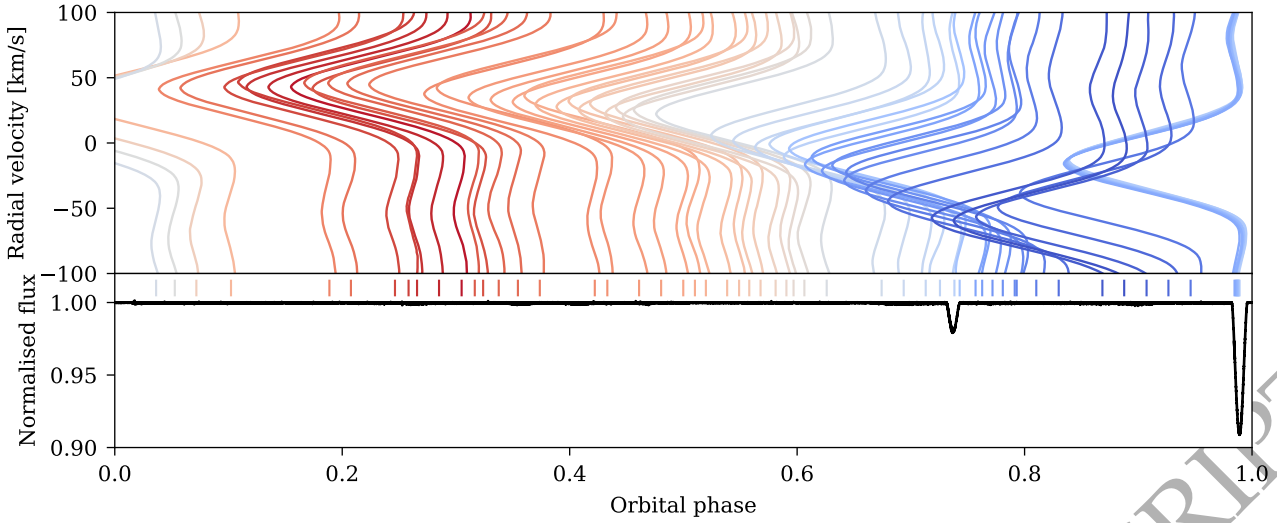


Figure 2. Top: Cross-correlation of each *SONG* spectrum against the constructed template. Each cross-correlation is coloured by its Doppler shift. Bottom: *TESS* light curve of α Dra folded on the orbital period. The coloured vertical lines above the light curve indicate orbital phases where *SONG* spectra were obtained. 

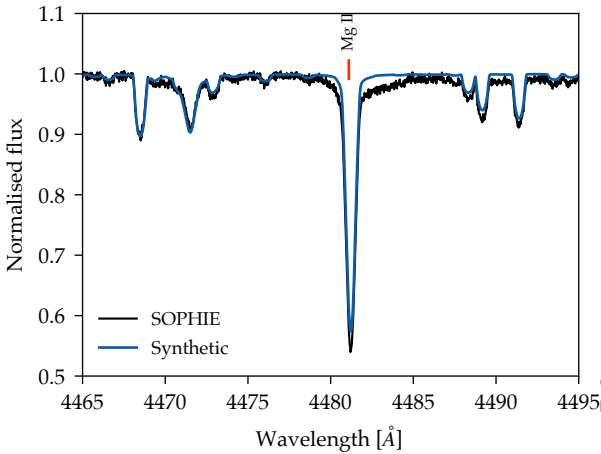


Figure 3. *SOPHIE* spectrum of α Dra in black with the best-fitting spectrum obtained in section overlaid in red. The broad feature near the Mg II line (4481 Å) is potentially caused by the rapidly rotating secondary. 

free and let `FDBINARY` optimize it. As with the iterative shift and stack, the resulting spectrum did not show any discernible stellar features.

Finally, we attempted to increase the signature of the secondary by applying Least-Squares Deconvolution (LSD) to the *SONG* spectra. In brief, this method builds an average, deconvolved line profile of all the lines within a given wavelength range from a selected line mask (Donati et al. 1997). While the classical LSD methodology relies on a single mask and single component to the average profile, we use the generalised LSD approach introduced by Tkachenko et al. (2013), which allows for the computation of multiple stellar components from the same spectrum using different line lists. In this way, we can compute the average profile of each component without compromising or suppressing the signal of the other component. We computed the LSD profiles for two stellar components using three LSD components each, from 4290 Å to 5600 Å. We used a synthetic line list computed from the Vienna Atomic Line Database (VALD-

II, Kupka et al. 1999), using the atmospheric parameters derived in Sec. 4. Similar to our other attempts, we could not reliably detect the presence of the secondary in the LSD profiles, despite the expected $\sim 15\%$ light contribution.

3 BINARY MODELLING

We simultaneously modelled the *TESS* photometry and radial velocity measurements to determine the fundamental parameters of the system. To perform the fit, we utilised the `ELLC` eclipsing binary code (Maxted 2016), wrapped in the Markov Chain Monte Carlo (Goodman & Weare 2010) ensemble sampling code: `EMCEE` (Foreman-Mackey et al. 2013).

3.1 ELLC setup

The free parameters in our model were: the orbital period (P_{orb}), the sum of the fractional radii ($r_{\text{sum}} = (R_1 + R_2)/a$, where a is the semi-major axis of the orbit), the ratio of radii (R_2/R_1), the orbital inclination (i), reference time of primary eclipse (T_0), the surface brightness ratio averaged over both stellar disks in the *TESS* band (S_T), the semi-major axis of the primary (a_1), the eccentricity (e) and periaapsis (ω) parametrised such that $f_c = \sqrt{e} \cos \omega$ and $f_s = \sqrt{e} \sin \omega$, the systemic velocity for each RV data-set ($\gamma_{v,(\text{SONG}, \text{Bischoff})}$), and the quadratic limb-darkening parameters ($q_{i,j}$). Priors on the time of primary eclipse, orbital period, and periaapsis were chosen to be a narrow uniform prior centred around the values from Bischoff et al. (2017). For the limb-darkening parameters, we used the efficient sampling method from Kipping (2013) with uniform priors between 0 and 1.

Before sampling our model with `EMCEE`, we examined whether we could extract mass and temperature information from the light curve. For α Dra, the *TESS* photometry exhibits clear v-shaped eclipses indicative of a grazing eclipsing system. In a detached binary with grazing eclipses, the light curve is insensitive to the mass ratio. Photometric mass ratios can be determined accurately for completely eclipsing binaries, which break the degeneracy between

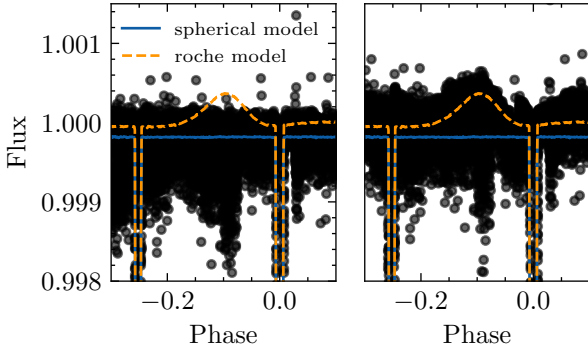


Figure 4. Sphere and Roche surface geometry models compared to two different methods of detrending of the *TESS* light curve. Left: light curve used in the ELLC setup. Right: light curve used in the PHOEBE setup. Both panels also show the PHOEBE models computed with spherical and Roche geometry of the stellar surfaces. 

the radii and inclination (Terrell & Wilson 2005). Photometric mass ratios can also be obtained for short-period binaries with ellipsoidal variations (i.e., contact and overcontact binaries). However, for a detached grazing system with no out-of-eclipse variability, the mass ratio only indirectly affects the limb darkening values used. We utilised a limb-darkening lookup table produced by Claret (2017) generated with the PHOENIX atmosphere models (Husser et al. 2013) for a square root limb-darkening law to attempt to fit the temperature and mass of both stars. In practice, however, the limb-darkening coefficients vary by less than 0.1% in the temperature region of interest. We performed a linear interpolation on the table and attempted to fit the light curve by adjusting the temperature and masses of the components. We found the result to be very poorly constrained, so we chose not to attempt a fit for temperature and mass in the model.

There is a clear anomaly in the radial velocity measurements during primary eclipse (inset of Fig. 6) which we attribute to the Rossiter-McLaughlin (RM) effect. We fitted for this in the ELLC model by allowing the projected rotational velocity, $v \sin i$, to be a free parameter. For the primary star, we used a uniform prior on $v \sin i$ of $U \sim (10, 50)$, initialised on the value of 26.2 km/s, which was taken from spectral analysis performed by Gray (2014).

Recent work has shown that significant degeneracies exist in the parameter space of eclipsing binary models (Prša & Zwitter 2005). Such degeneracies often lead to sampling of a local minimum as opposed to the correct parameter values. To avoid this, we initialised the parameters for sampling by using a differential evolution algorithm, which aims to find the global minimum of the parameter space (Storn & Price 1997). Differential evolution is a costly algorithm which requires many evaluations of the model, so we only applied it to every 20th data point in the in-eclipse light curve. We used several other techniques to speed-up computation as follows. Since the system is well detached, we modelled both components as spheres. We further fitted only the in-eclipse flux data since the light curve is essentially constant out of eclipse. After obtaining a good initial fit, we ran the EMCEE sampler with 70 walkers for 15,000 steps, with 10,000 steps of burn-in. After sampling, we found that the final values were almost identical to the initial values used.

3.2 PHOEBE setup

To test our assumption of spherical geometry for the two stars from the ELLC modelling, we also computed a model with Roche geometry using the results in Table 2. We note a prominent periastron brightening feature both in the model and data which was suppressed in the original detrending for the ELLC model (Figure 4). This called for an additional step in the modeling with a more robust setup. For this purpose, we used PHOEBE, whose latest release (Conroy et al. 2020) supports fitting, including sampling with MCMC and adding distributions as priors to any model parameter. PHOEBE is a powerful binary modelling software written in PYTHON, which aims to provide a full physical description of both stars and the binary orbit.

We initialized all relevant parameters in their values from Table 2. Because PHOEBE relies on a different, and much larger, set of parameters, some of the ELLC parameters do not have direct equivalents in the PHOEBE model. We reparametrised f_c and f_s as $e \cos \omega$ and $e \sin \omega$, the surface brightness ratio S_T as the temperature ratio $T_{\text{eff},2}/T_{\text{eff},1}$ and $v \sin i$ as the synchronicity parameter (the ratio between the rotational and orbital angular velocities) of the primary F_1 . We also used only the *SONG* radial velocity curve and fit for the systemic velocity v_γ . In addition, we marginalized over the mass ratio q , effective temperature of the primary $T_{\text{eff},1}$, passband luminosity of the primary L_{pb} (defined as the product of the surface brightness and area of the stellar disk, Kallrath & Milone 2009) and synchronicity parameter of the secondary F_2 .

Unlike ELLC, PHOEBE offers support for interpolating limb-darkening coefficients directly from atmosphere tables (Prša et al. 2016), which provides a self-consistent treatment of the distribution of brightness across the stellar surface. Therefore, we marginalised over the effective temperature of the primary, as well as the gravity darkening coefficients ($\beta_{1,2}$) and albedoes ($A_{1,2}$) for both stars, to account for potential model uncertainties in the distribution of intensities across the stellar surface. As such, the reported temperature from the PHOEBE fit should not be taken as a final value, in particular because the metallicity of both stars was fixed at solar and a more advanced treatment is required for abundance analysis and temperature estimation (see Section 4.1).

The triangulated mesh of the stellar surfaces in PHOEBE introduces a certain level of model noise, which can be decreased by increasing the number of triangles required to cover a stellar surface. To optimize the computational cost required to sample this robust model with MCMC, we modelled the primary star with Roche geometry and ~ 3000 triangles, while the secondary was modeled with spherical geometry and ~ 1500 triangles. To further reduce the computational time of the PHOEBE model, we resampled the *TESS* light curve to every 20th point in the regions of the eclipses and periastron brightening, and to every 5000th point elsewhere. We ran EMCEE through the PHOEBE wrapper with an initial run of 72 walkers and 600 iterations, and a final MCMC run using 192 walkers and 1200 iterations (initialized in the previous sample), with 600 iterations of burn-in.

3.3 Results

We show the best fitting models in Fig. 5 and Fig. 6 for the light and radial velocity curves, respectively, and corner plots of the directly sampled parameters in Appendix A1. The median value of the posterior probability for each parameter is reported in Table 2, for the ELLC and PHOEBE models, along with uncertainties at the 16th and 84th percentiles of the posterior distribution.

From Fig. 5, there is clearly some eclipse-to-eclipse variabil-

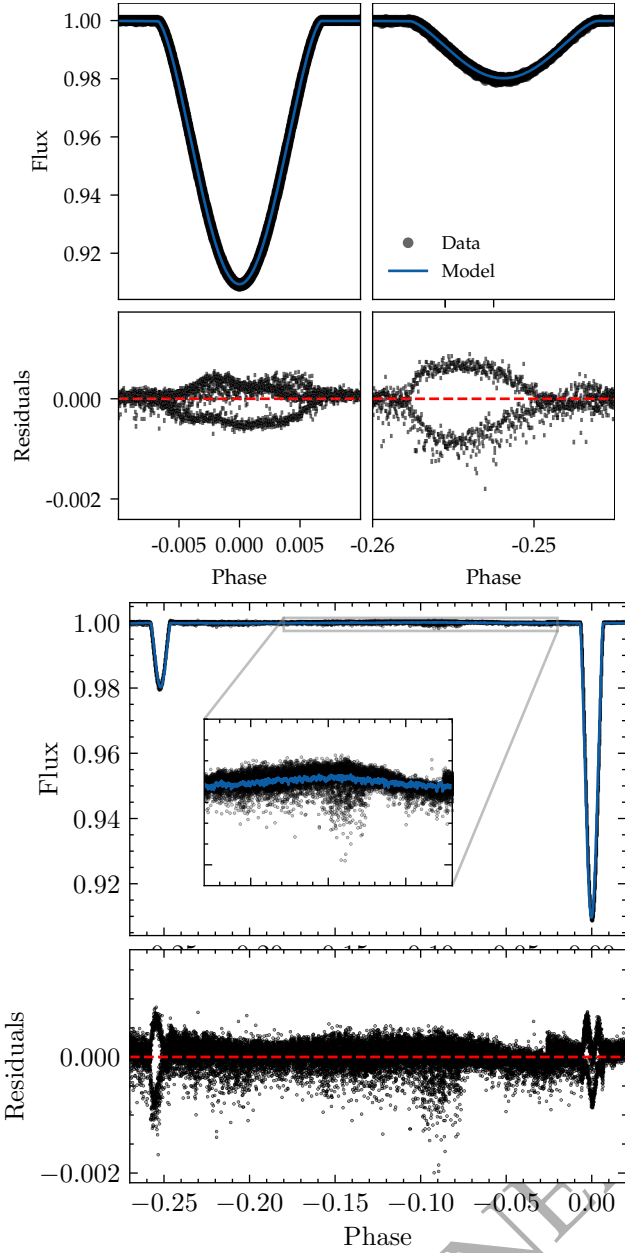


Figure 5. Top: ELCC fit to the light curve shown for the primary and secondary phase folded eclipses. Note that the phase has been corrected so that the primary eclipse occurs at a phase of 0. Bottom: PHOEBE fit to the light curve. The inset shows the variation in the flux level out of eclipse as modelled by the PHOEBE Roche model. The notable scatter in the PHOEBE model out of eclipse is a consequence of the model noise caused by the triangulated mesh.

ity that is not accounted for by the light curve model. We tried several techniques to account for this, including fitting for apsidal motion, fixing the limb-darkening parameters to set values, and re-processing the target pixel file with other methods. However, we were unable to remove the residual signal. We believe its most likely origin is due to the detrending of the light curve, which was only performed out of eclipse. Any variations in the eclipses were thus retained in the final light curve. Alternatively, the origin of these residuals could be either a background star that was included by

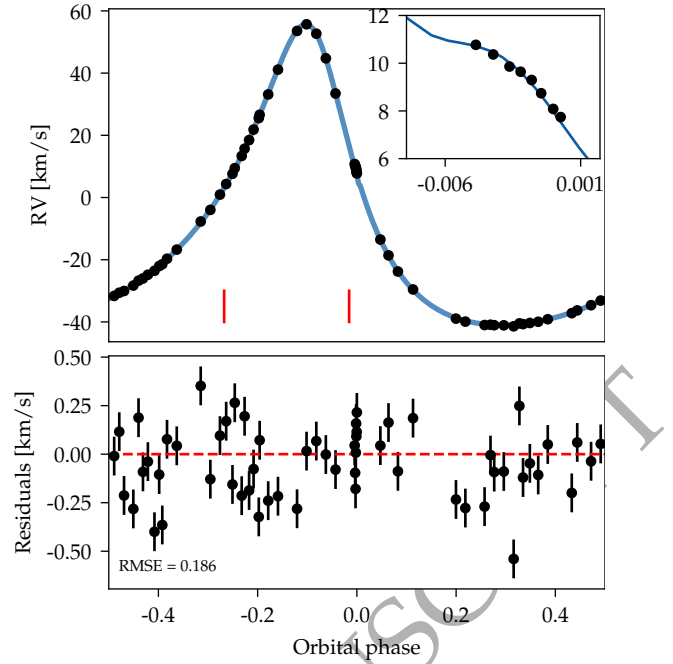


Figure 6. Fit to the radial velocity curve of the primary star. The top panel shows the data (black points) and best-fitting model (blue line). The orbital phase has been defined so that primary eclipse occurs at phase 0, with the phases of primary and secondary eclipse being marked in red. The inset shows the zoomed fit to the Rossiter-McLaughlin effect during primary eclipse. The bottom panel shows the residuals (observed minus calculated) with the calculated root mean square error (RMSE). Points are shown for the SONG RVs only.

the aperture mask, or red noise inherent in the *TESS* data, because the shape of the eclipse changes marginally every orbital period. However, since the residual flux is less than 0.2% of the total flux, it is unlikely to strongly affect the resulting parameters.

The fitted $v \sin i$ of the model was found to be 36.8 ± 2.3 km/s, a value significantly higher than the 26.2 ± 0.2 km/s reported by (Gray 2014). This discrepancy is probably due to the poor phase coverage of the RM effect in our RVs. The value reported by Gray (2014) is obtained from precise spectral line measurements, which is far more accurate.

The results of the separate *ELLCC* and *PHOEBE* modelling are close for the parameters that can be compared. Most notably, it appears that the *PHOEBE* model yielded slightly lower uncertainties on most of the parameters. This could be a result of the more accurate prescription of the stellar modelling employed by *PHOEBE*, as well as the additional priors and default *PHOEBE* parameter constraints. The inclusion of the periastron brightening feature in the light curve modeled with *PHOEBE* also helps better constrain the solution. We note that the differences in some parameter values are most likely due to the fact that the *ELLCC* and *PHOEBE* models employ different stellar geometries (spherical and roche).

4 ANALYSIS OF THE PRIMARY

We determined the effective temperature (T_{eff}) and surface gravity ($\log g$) of α Dra A using the *UVBYBETA* code developed by Napiwotzki et al. (1993). This code is based on the Moon & Dworetzky (1985) grid, which calibrates the *uvby β* photometry in terms of T_{eff} and $\log g$. The derived effective temperature

Parameter	ELLC Prior	PHOEBE Prior	ELLC value	PHOEBE value	Unit
P_{orb}	U~(50.4, 52.4)	U~(50.4, 52.4)	$51.41886^{+0.00008}_{-0.00008}$	$51.418946^{+0.00006}_{-0.00006}$	day
$(R_1 + R_2)/a$	U~(0.001, 0.1)	U~(0.001, 0.1)	$0.0704^{+0.0005}_{-0.0004}$	$0.070092^{+0.0007}_{-0.0007}$	
R_2/R_1	U~(0.1, 0.9)	U~(0.1, 0.9)	$0.47^{+0.01}_{-0.01}$	$0.463^{+0.003}_{-0.003}$	
i	U~(45, 90)	U~(80, 90)	$86.35^{+0.04}_{-0.04}$	$86.365^{+0.006}_{-0.006}$	deg
T_0	U~(2458695, 2458697)	U~(2458695, 2458697)	$2458696.0199^{+0.0002}_{-0.0002}$	$2458696.02599^{+0.0002}_{-0.0002}$	BJD
a_1	U~(10, 150)	U~(10, 150)	$44.59^{+0.1}_{-0.1}$	$44.54^{+0.04}_{-0.04}$	R_{\odot}
ELLC only parameters	Prior	Value			
$\sqrt{e} \cos \omega$	U~(0.5, 0.7)	$0.6068^{+0.0003}_{-0.0003}$			
$\sqrt{e} \sin \omega$	U~(0.07, 0.3)	$0.237^{+0.002}_{-0.001}$			
γ_V, SONG	U~(-20, -5)	$-11.76^{+0.03}_{-0.03}$			km/s
$\gamma_V, \text{Bischoff}$	U~(-20, -5)	$-13.5^{+0.1}_{-0.1}$			km/s
S_T	U~(0.01, 1.5)	$1.02^{+0.04}_{-0.03}$			
$v \sin i$	U~(10, 50)	$36.8^{+2.3}_{-2.3}$			km/s
q_{11}	U~(0.0, 1.0)	$0.17^{+0.1}_{-0.05}$			
q_{12}	U~(0.0, 1.0)	$0.5^{+0.3}_{-0.3}$			
q_{21}	U~(0.0, 1.0)	$0.2^{+0.2}_{-0.1}$			
q_{22}	U~(0.0, 1.0)	$0.4^{+0.3}_{-0.3}$			
PHOEBE only parameters	Prior	Value			
$T_{\text{eff},2}/T_{\text{eff},1}$	U~(0.01, 1.5)	$1.0045^{+0.008}_{-0.007}$			
$e \sin \omega$	U~(-1, 1)	$0.15245^{+0.001}_{-0.0006}$			
$e \cos \omega$	U~(-1, 1)	$0.395319^{+0.00006}_{-0.00006}$			
v_{γ}	U~(-20, -5)	$-11.755^{+0.03}_{-0.03}$			km/s
F_1	U~(0.01, 10)	$4.4^{+0.4}_{-0.40}$			
F_2	U~(0.01, 100)	42^{+16}_{-12}			
$T_{\text{eff},1}$	U~(7500, 15000)	11740.0^{+270}_{-430}			
q	U~(0.1, 1.1)	$0.37^{+0.05}_{-0.05}$			
L_{pb}	U~(2, 20)	$10.35^{+0.03}_{-0.03}$			W
β_1	U~(0, 1)	$0.25^{+0.15}_{-0.12}$			
β_2	U~(0, 1)	$0.51^{+0.28}_{-0.21}$			
A_1	U~(0, 1)	$0.59^{+0.12}_{-0.17}$			
A_2	U~(0, 1)	$0.58^{+0.14}_{-0.20}$			
Derived quantities	ELLC Prior	PHOEBE Prior	ELLC value	PHOEBE value	Unit
R_1/a			$0.0479^{+0.0003}_{-0.0002}$	$0.0479^{+0.0004}_{-0.0004}$	
R_2/a			$0.0225^{+0.0005}_{-0.0005}$	$0.02220^{+0.0002}_{-0.0002}$	
K_1			$47.77^{+0.06}_{-0.06}$	$47.85^{+0.05}_{-0.05}$	km/s
e			$0.4241^{+0.0003}_{-0.0003}$	$0.4234^{+0.0003}_{-0.0003}$	
ω			$0.372^{+0.002}_{-0.002}$	$0.368^{+0.002}_{-0.002}$	rad

Table 2. All parameters used in the combined photometric and radial velocity model, including their priors for both the ELLC and PHOEBE models. The reported values are the median result of the MCMC chain, with uncertainties reported as the 16th and 84th percentiles of the posterior distribution. As a result of differing models, the table is separated according to whether the parameter is in both models or just one. The derived quantities are parameters that were obtained from these parameters – individual masses and radii were unavailable from the ELLC model and are thus left blank.

is $T_{\text{eff}} = 9975 \pm 125$ K and $\log g = 3.63 \pm 0.20$ dex. These values are identical to those of (Adelman et al. 2011), who derived them via the same method.

We also modelled the photometry by fitting to MIST stellar isochrones with the ISOCHRONES package (Morton 2015). We simultaneously fit a combination of Gaia, WISE, 2MASS, and

StrÅumgren photometry, using a Markov chain Monte-Carlo nested sampling approach to find the best-fitting atmospheric parameters (PyMultinest; Buchner et al. 2014). Uncertainties on the constraints were included as priors in the Bayesian fitting process and were thus propagated to the final results. We attempted to fit both a single and a binary star isochrone model using the UVBYBETA-derived

temperature and surface gravity as priors. For the fit, we used the Hipparcos parallax of 10.76 ± 0.17 mas (van Leeuwen 2007) because it has slightly lower uncertainties than the latest Gaia eDR3 parallax (10.52 ± 0.20 mas; Collaboration et al. 2021). Fitting the photometry as a binary system yielded no useful results. Indeed, this is not unexpected because the secondary only accounts for around 15% of the total flux of α Dra. On the other hand, the single star fit was well-constrained by the tight priors on temperature and surface gravity, and yielded the mass and radius of the primary to be $3.71^{+0.09}_{-0.07} M_{\odot}$ and $5.8^{+0.1}_{-0.1} R_{\odot}$ respectively. The luminosity of the system was found to be $\log(L/L_{\odot}) = 2.49 \pm 0.02$.

Kallinger et al. (2004) have suggested that α Dra A is photometrically variable, with a period of about 53 min and an amplitude of 1-2 mmag. They speculated that α Dra could belong to the unconfirmed class of so-called ‘Maia variables’, lying between the blue edge of the instability strip of δ Scuti stars and the red edge of slowly pulsating B-type stars (White et al. 2017). As noted by Bedding et al. (2019), we see no evidence for photometric variability in α Dra (beyond eclipses), and can rule out variability on timescales shorter than 8 hr at the precision of 10 parts per million (ppm) from the eclipse subtracted light curve.

4.1 Abundance analysis

To determine elemental abundances, we retrieved previous observations of α Dra from the *SOPHIE* archive hosted at Observatoire de Haute Provence. *SOPHIE* is an échelle spectrograph that, in its high resolution mode ($R = 75000$), yields a full spectral coverage from 3820 Å to 6930 Å in 39 orders (Perruchot et al. 2008). We chose to analyse the single available *SOPHIE* spectrum as opposed to the newly collected *SONG* spectra since *SOPHIE* possesses a wider spectral coverage at a higher SNR. The spectra were extracted online from the detector images using a pipeline adapted from the High Accuracy Radial Velocity Planet Searcher (*HARPS*). We normalized each reduced order separately using a Chebyshev polynomial fit with sigma clipping, rejecting points outside one standard deviation of the local continuum. Normalized orders were then merged, corrected by the blaze function, and re-sampled into a constant wavelength step of 0.02 Å (see Royer et al. 2014, for more details). The single *SOPHIE* spectrum was not included in the RV analysis.

We derived the abundances of 21 chemical elements by iteratively adjusting synthetic spectra to the normalized spectrum and looking for the best fit to carefully selected unblended lines. The atomic linelist was constructed following Monier et al. (2019). Synthetic spectra were computed assuming LTE using Hubeny & Lanz (1992) *SYNSPEC49* code, which calculates lines for elements up to $Z=99$. In order to derive the microturbulent velocity, we simultaneously derived the iron abundance [Fe/H] for fifty unblended Fe-II lines and a set of microturbulent velocities ranging from 0.0 to 2.0 km/s. The adopted microturbulent velocity is the value which minimizes the standard deviations, that is, for that value, all Fe-II lines yield the same iron abundance. We found a null microturbulent velocity within a precision of 0.1 km/s, a result consistent with the value found by Adelman et al. (2011).

4.2 Model atmospheres

The *ATLAS9* code (Kurucz 1992) was used to compute a first model atmosphere for the effective temperature and surface gravity of α Dra A ($T_{\text{eff}}=9975$ K and $\log g=3.63$ obtained with *UVBYBETA*)

Table 3. Atmospheric composition of the primary star of α Dra. We here refer to the absolute abundance in the star: $\log_{10} \left(\frac{X}{H} \right)_{\star}$. The third column shows the corresponding solar abundance and the number of lines analysed is in the fourth column.

Ion	Absolute abundance	Solar abundance	Number of lines
He	-1.17 ± 0.45	-1.070	2
C	-3.63 ± 0.34	-3.61	3
O	-3.22 ± 0.19	-3.34	9
Na	-5.67 ± 0.20	-5.67	4
Mg	-4.47 ± 0.29	-4.42	3
Al	-5.53 ± 0.20	-5.53	2
Si	-4.60 ± 0.09	-4.45	6
P	-6.55 ± 0.16	-6.55	3
S	-4.67 ± 0.16	-4.67	3
Ca	-5.79 ± 0.17	-5.64	2
Sc	-9.23 ± 0.20	-8.83	3
Ti	-6.92 ± 0.06	-6.98	10
V	-7.56 ± 0.23	-8.00	3
Cr	-6.25 ± 0.17	-6.33	6
Mn	-6.61 ± 0.08	-6.61	2
Fe	-4.60 ± 0.16	-4.50	11
Ni	-6.35 ± 0.27	-5.75	2
Sr	-9.55 ± 0.20	-9.03	2
Y	-9.16 ± 0.20	-9.16	2
Zr	-9.40 ± 0.20	-9.40	4
Ba	-9.87 ± 0.22	-9.87	3

assuming a plane parallel geometry, a gas in hydrostatic and radiative equilibrium and local thermodynamical equilibrium. The *ATLAS9* model atmosphere contains 72 layers with a regular increase in $\log \tau_{\text{Ross}} = 0.125$ and was calculated assuming a solar chemical composition (Grevesse & Sauval 1998). It was converged up to $\log \tau = -5.00$ in order to attempt reproduce the cores of the Balmer lines. This *ATLAS9* version uses the new opacity distribution function of Castelli & Kurucz (2004) computed for that solar chemical composition. Once a first set of elemental abundances were derived using the *ATLAS9* model atmosphere, the atmospheric structure was recomputed for these abundances using the opacity sampling *ATLAS12* code (Kurucz 2013). Slightly different abundances were then derived and a new *ATLAS12* model was recomputed until the abundances in subsequent iterations differed by less than ± 0.10 dex.

Only unblended lines are used to derive the final abundances. The reported abundance is given as a weighted mean of the abundances derived for each transition. For several of the heaviest elements, only one unblended was available from which to calculate the abundance. Thus, these values should be considered uncertain at best. For each transition, the adopted abundance is that which provides the closest match to the normalized profile as calculated by *SYNSPEC49* (Hubeny & Lanz 1992). The computations were performed by varying the unknown abundance values until χ^2 was minimised between the observed and synthetic spectrum. The final abundances of α Dra and their error bars are listed in Table 3. These error bars were calculated to be the standard deviations of individual measurements around the mean abundance.

5 DISCUSSION AND CONCLUSIONS

A0 III is a rare spectral type. It has been suggested to be a transitional state between two types of chemically peculiar A stars

(Adelman et al. 1987). As a result, it is challenging to determine fundamental parameters. To the best of our knowledge, only two other eclipsing binaries are known to host A0 III type stars: V452 Mon and V1461 Aql (Sebastian et al. 2012).

Given the obtained mass function and mass of the primary, we estimate the secondary to have a minimum mass of around $2.50 \pm 0.14 M_{\odot}$, which corresponds to an A2V spectral type with a luminosity of around $L = 40 L_{\odot}$. This is in slight disagreement with the results of the PHOEBE modelling, which provided a secondary mass of $2.88 \pm 0.04 M_{\odot}$, indicating that one or both of the parameters have underestimated uncertainties. Despite this, the luminosity is in good agreement with the known secondary contribution of 15.6% to the total flux of α Dra. The fact that the secondary remains undetected in the spectra could be explained by a rapid rotational velocity. If the secondary is an A-type star, as suggested by modelling, then it is likely to have a high $v \sin i$ which would lead to broadening of the spectral lines as seen in Fig. 3. For a mass of $2.50 M_{\odot}$, the bimodal distribution of rotational velocities peaks at both 50 and 200 km/s (Zorec & Royer 2012), supporting our argument for a rapidly rotating companion.

Using the results of Southworth et al. (2007), we can also estimate the surface gravity of the secondary from the orbital period (P), the RV semi-amplitude of the primary (K_1), eccentricity (e), inclination (i), and fractional radius of the secondary (R_2/a):

$$g = \frac{2\pi (1 - e^2)^{1/2} K_1}{P (R_2/a)^2 \sin i}. \quad (1)$$

Using this, with the values of the ELLC fit from Table 2, we find the surface gravity of the secondary to be 4.08 ± 0.02 dex.

If we consider abundances which depart by more than ± 0.20 dex (a usual accuracy for abundances) to be non-solar, then only three elements are truly under-abundant in α Dra: scandium (by a factor of 0.40 times the solar abundance), nickel (0.25) and strontium (0.30). Only vanadium is truly overabundant by a factor of 2.75. The abundances of the other elements do not differ significantly from solar. The abundance pattern of α Dra appears to be a combination of nearly solar abundances for most elements and under-abundances for only three elements. It differs from the metal poor status found by Adelman et al. (2001) possibly because the atomic data have changed since then. Whether this pattern was present at the formation of the star or is the result of stellar evolution is an open question. Note also that the peculiar nature of α Dra is listed by Renson & Manfroid (2009a) as being unconfirmed by later observations.

Future measurements of this system could improve the precision on the fundamental properties. Interferometry to obtain the angular diameters of both stars would yield the semi-major axis of the orbit and the mass ratio. If the secondary RVs could be extracted, almost all parameters in the system could be obtained. Finally, a complete astrometric orbit is expected from the impending release of Gaia DR3. This would provide independent measures of the mass ratio, radii, and semi-major axis of the orbit.

ACKNOWLEDGEMENTS

We are grateful to the TESS team for such excellent data. We thank the anonymous referee for their comments, which greatly improved the quality of the paper. We also thank Andrej Prsa for useful discussions, and Kyle Conroy for providing PHOEBE support. DRH gratefully acknowledges the support of the Australian Government Research Training Program (AGRTP) and University of Sydney

Merit Award scholarships. This research has been supported by the Australian Government through the Australian Research Council DECRA grant number DE180101104 and Discovery Project DP210103119. This research used observations made with the Hertzprung SONG telescope operated on the Spanish Observatorio del Teide on the island of Tenerife by the Aarhus and Copenhagen Universities and by the Instituto de Astrofísica de Canarias. Funding for the Stellar Astrophysics Center is provided by The Danish National Research Foundation (Grant agreement no. DNR106). This work has made use of the VALD database, operated at Uppsala University, the Institute of Astronomy RAS in Moscow, and the University of Vienna. CJ has received funding from the European Research Council (ERC) under the European Union's Horizon 2020 research and innovation programme (grant agreement N°670519; MAMSIE) and from the Research Foundation Flanders (FWO) under grant agreement and G0A2917N (BlackGEM).

This paper has made use of the following software not cited in the text: NUMPY (Oliphant 2015), SCIPY (Virtanen et al. 2019), ASTROPY (Price-Whelan et al. 2018), and LIGHTCURVE (Vincic et al. 2018).

DATA AVAILABILITY

The data underlying this article are available in the GitHub repository, at <https://github.com/danhey/adra>

REFERENCES

- Adelman S. J., Bolcal C., Kocer D., Inelmen E., 1987, *Publications of the Astronomical Society of the Pacific*, 99, 130
- Adelman S. J., Caliskan H., Kocer D., Kablan H., Yüce K., Engin S., 2001, *Astronomy and Astrophysics*, 371, 1078
- Adelman S. J., Yu K., Gulliver A. F., 2011, *Astronomische Nachrichten*, 332, 153
- Andersen J., 1991, *The Astronomy and Astrophysics Review*, 3, 91
- Andersen M. F., et al., 2014, pp 83–86
- Andersen M. F., et al., 2019, *Astronomy & Astrophysics*, 623, L9
- Bedding T. R., Hey D. R., Murphy S. J., 2019, *Research Notes of the AAS*, 3, 163
- Behr B. B., Hajian A. R., Cenko A. T., Murison M., McMillan R. S., Hindsley R., Meade J., 2009, *The Astrophysical Journal*, 705, 543
- Bischoff R., et al., 2017, *Astronomische Nachrichten*, 338, 671
- Blanco-Cuarezma S., Soubiran C., Heiter U., Jofré P., 2014, *Astronomy & Astrophysics*, 569, A111
- Buchner J., et al., 2014, *Astronomy & Astrophysics*, 564, A125
- Campbell W. W., Curtis H. D., 1903, *The Astrophysical Journal*, 18, 306
- Castelli F., Kurucz R. L., 2004, arXiv:astro-ph/0405087
- Claret A., 2017, *Astronomy & Astrophysics*, 600, A30
- Collaboration G., et al., 2021, *Astronomy and Astrophysics*, 649, A1
- Conroy K. E., et al., 2020, *The Astrophysical Journal Supplement Series*, 250, 34
- Donati J.-F., Semel M., Carter B. D., Rees D. E., Collier Cameron A., 1997, *Monthly Notices of the Royal Astronomical Society*, 291, 658
- Foreman-Mackey D., Hogg D. W., Lang D., Goodman J., 2013, *Publications of the Astronomical Society of the Pacific*, 125, 306
- Goodman J., Weare J., 2010, *Communications in Applied Mathematics and Computational Science*, 5, 65
- Gray D. F., 2014, *The Astronomical Journal*, 147, 81
- Grevesse N., Sauval A. J., 1998, *Space Science Reviews*, 85, 161
- Hadrava P., 1995, *Astronomy and Astrophysics Supplement Series*, 114, 393
- Higl J., Weiss A., 2017, *Astronomy & Astrophysics*, 608, A62
- Hubeny I., Lanz T., 1992, *Astronomy and Astrophysics*, 262, 501

- Husser T.-O., Wende-von Berg S., Dreizler S., Homeier D., Reiners A., Barman T., Hauschildt P. H., 2013, *Astronomy and Astrophysics*, 553, A6
- Hutter D. J., Zavala R. T., Tycner C., Benson J. A., Hummel C. A., Sanborn J., Franz O. G., Johnston K. J., 2016, *The Astrophysical Journal Supplement Series*, 227, 4
- Ilijic S., Hensberge H., Pavlovski K., Freyhammer L. M., 2004, pp 111–113
- Kallinger T., Iliev I., Lehmann H., Weiss W. W., 2004, *Proceedings of the International Astronomical Union*, 2004, 848
- Kallrath J., Milone E. F., 2009, *Eclipsing Binary Stars: Modeling and Analysis*, 2 edn. Astronomy and Astrophysics Library, Springer-Verlag, New York
- Kipping D. M., 2013, *Monthly Notices of the Royal Astronomical Society*, 435, 2152
- Kupka F., Piskunov N., Ryabchikova T. A., Stempels H. C., Weiss W. W., 1999, *Astronomy and Astrophysics Supplement Series*, 138, 119
- Kurucz R. L., 1992, *Revista Mexicana de Astronomia y Astrofisica*, vol. 23, 23
- Kurucz R. L., 2013, *Astrophysics Source Code Library*, p. ascl:1303.024
- Mahy L., Gosset E., Sana H., Damerdjy Y., De Becker M., Rauw G., Nitschelm C., 2012, *Astronomy and Astrophysics*, 540, A97
- Maxted P. F. L., 2016, *Astronomy & Astrophysics*, 591, A111
- Maxted P. F. L., et al., 2020, *Monthly Notices of the Royal Astronomical Society*, 498, 332
- Monier R., Griffin E., Gebran M., Kılıçoğlu T., Merle T., Royer F., 2019, *The Astronomical Journal*, 158, 157
- Moon T. T., Dworetsky M. M., 1985, *Monthly Notices of the Royal Astronomical Society*, 217, 305
- Morton T. D., 2015, *Astrophysics Source Code Library*, p. ascl:1503.010
- Napiwotzki R., Schoenberner D., Wenske V., 1993, *Astronomy and Astrophysics*, 268, 653
- Oliphant T. E., 2015, *Guide to NumPy*, 2nd edn. CreateSpace Independent Publishing Platform, USA
- Pavlovski K., Hensberge H., 2010, p. 207
- Perruchot S., et al., 2008, in *Ground-Based and Airborne Instrumentation for Astronomy II*. International Society for Optics and Photonics, p. 70140J, doi:10.1117/12.787379
- Price-Whelan A. M., et al., 2018, *The Astropy Project: Building an Open-Science Project and Status of the v2.0 Core Package*
- Prša A., Zwitter T., 2005, *The Astrophysical Journal*, 628, 426
- Prša A., et al., 2016, *The Astrophysical Journal Supplement Series*, 227, 29
- Renson P., Manfroid J., 2009a, *Astronomy and Astrophysics*, 498, 961
- Renson P., Manfroid J., 2009b, *VizieR Online Data Catalog*, 3260
- Ricker G. R., et al., 2014, *Journal of Astronomical Telescopes, Instruments, and Systems*, 1, 014003
- Royer F., et al., 2014, *Astronomy and Astrophysics*, 562, A84
- Sebastian D., Guenther E. W., Schaffenroth V., Gandolfi D., Geier S., Heber U., Deleuil M., Moutou C., 2012, *Astronomy and Astrophysics*, 541, A34
- Shenar T., et al., 2020, *Astronomy and Astrophysics*, 639, L6
- Smith J. C., et al., 2012, *Publications of the Astronomical Society of the Pacific*, 124, 1000
- Southworth J., Wheatley P. J., Sams G., 2007, *Monthly Notices of the Royal Astronomical Society*, 379, L11
- Stassun K. G., Hebb L., López-Morales M., Prša A., 2009, *The Ages of Stars*, 258, 161
- Storn R., Price K., 1997, *Journal of Global Optimization*, 11, 341
- Terrell D., Wilson R., 2005, in Drechsel H., Zejda M., eds., *Zdeněk Kopal's Binary Star Legacy*. Springer Netherlands, Dordrecht, pp 221–230, doi:10.1007/1-4020-3875-5_30
- Tkachenko A., Reeth T. V., Tsybal V., Aerts C., Kochukhov O., Debosscher J., 2013, *Astronomy & Astrophysics*, 560, A37
- Torres G., Andersen J., Giménez A., 2010, *Astronomy and Astrophysics Review*, 18, 67
- Vinícius Z., Barentsen G., Hedges C., Gully-Santiago M., Cody A. M., 2018, *KeplerGO/Lightkurve*
- Virtanen P., et al., 2019, arXiv e-prints, 1907, arXiv:1907.10121
- White T. R., et al., 2017, *Monthly Notices of the Royal Astronomical Society*, 471, 2882
- Zorec J., Royer F., 2012, *Astronomy and Astrophysics*, 537, A120
- van Leeuwen F., 2007, *Astronomy & Astrophysics*, 474, 653

APPENDIX A: CORNER PLOTS

This paper has been typeset from a $\text{\TeX}/\text{\LaTeX}$ file prepared by the author.

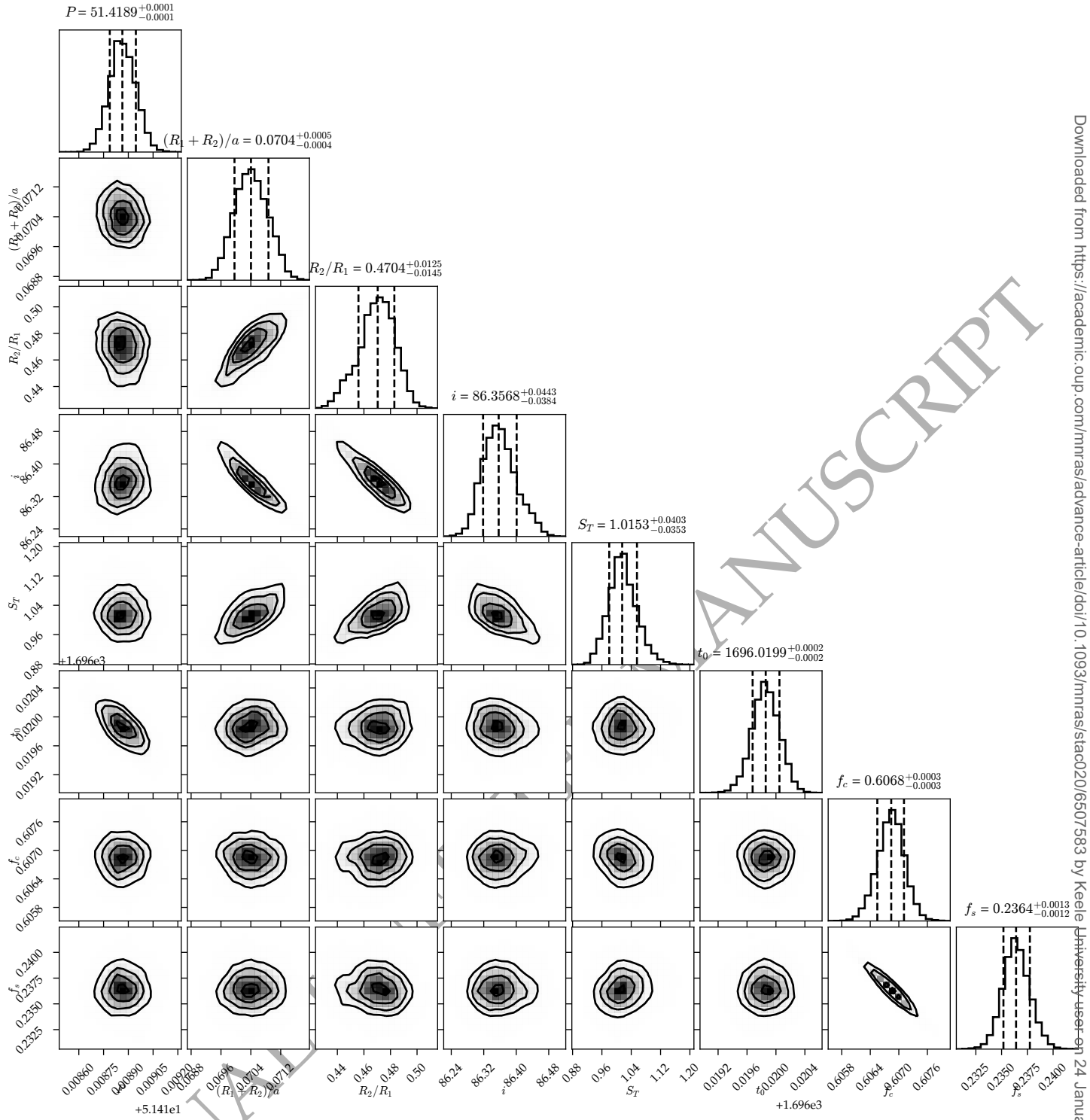


Figure A1. Corner plot of the posterior distributions for the combined light curve and RV model with ELLC. The dashed black lines correspond to the 16th, 50th, and 84th percentiles. Note that t_0 was sampled in Barycentric *TESS* Julian Date (BTJD), corresponding to BJD - 2457000. Not all parameters in the model have been shown.

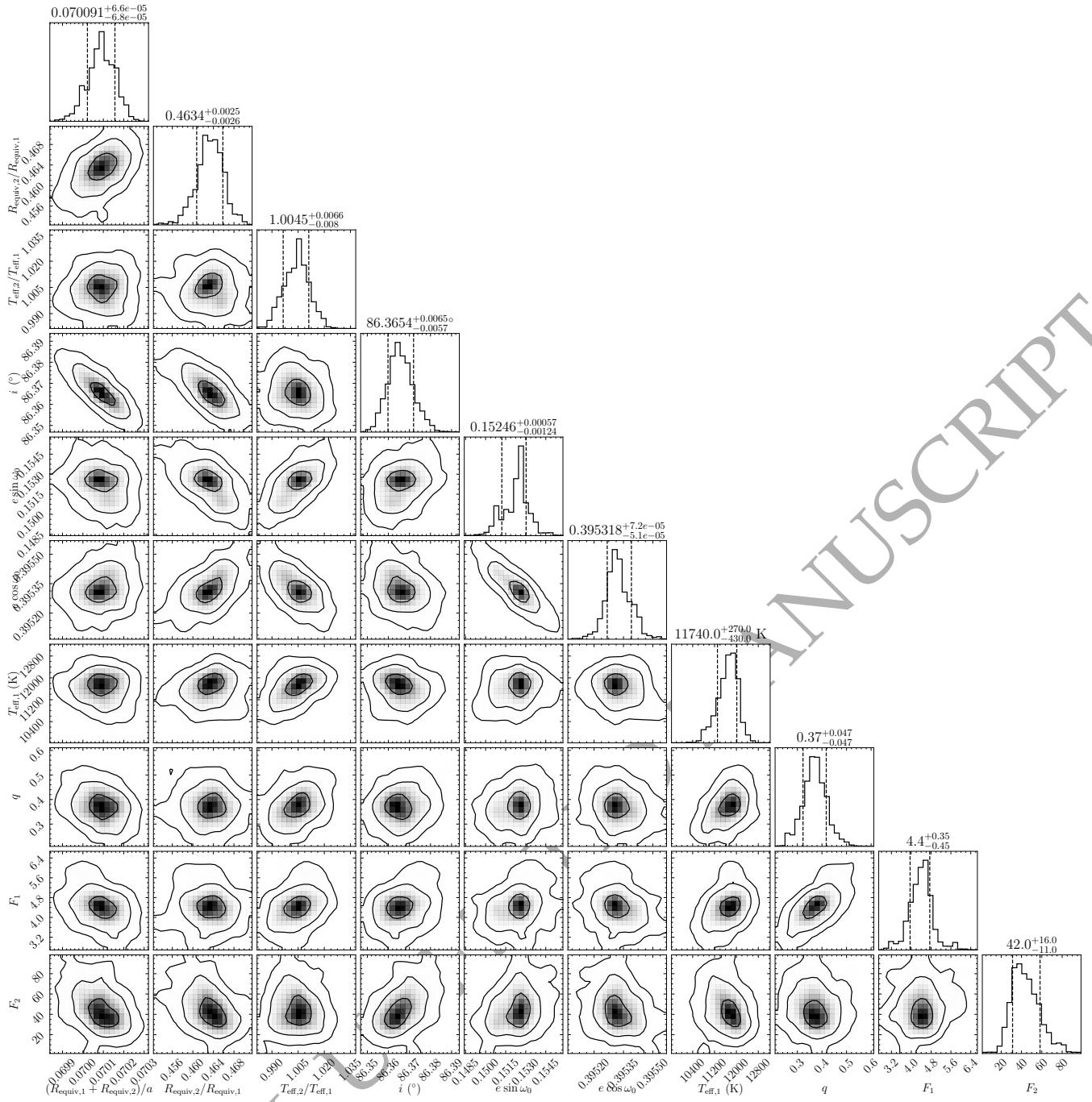


Figure A2. Corner plot of the posterior distributions for the combined light curve and RV model with PHOEBE. The dashed black lines correspond to the 16th, 50th, and 84th percentiles. Not all parameters in the model have been shown.